Evolution of real contact area under shear and the value of static friction of soft materials

R. Sahli[a], G. Pallares[a,b], C. Ducottet[c], I. E. Ben Ali[d], S. Al Akhrass[d], M. Guibert[a], and J. Scheibert[a,1]

[a]Laboratoire de Tribologie et Dynamique des Systèmes UMR5513, Université de Lyon, Ecole Centrale de Lyon, Ecole Nationale d'Ingénieurs de Saint-Etienne, Ecole Nationale des Travaux Publics de l'Etat, CNRS, F-69134 Ecully, France; [b]Laboratoire d'Innovation Numérique pour les Entreprises et les Apprentissages au service de la Compétitivité des Territoires, Centre des Etudes Supérieures Industrielles, F-34070 Montpellier, France; [c]Laboratoire Hubert Curien UMR5516, Université de Lyon, Université Jean Monnet Saint-Etienne, CNRS, Institut d'Optique Graduate School, F-42023 Saint-Etienne, France; and [d]Ingénierie des Matériaux Polymères UMR5223, CNRS, Université Claude Bernard Lyon 1, Université Jean Monnet Saint-Etienne, Université de Lyon, Institut National des Sciences Appliquées Lyon, F-69622 Villeurbanne, France

Edited by David A. Weitz, Harvard University, Cambridge, MA, and approved December 4, 2017 (received for review April 18, 2017)

The frictional properties of a rough contact interface are controlled by its area of real contact, the dynamical variations of which underlie our modern understanding of the ubiquitous rate-and-state friction law. In particular, the real contact area is proportional to the normal load, slowly increases at rest through aging, and drops at slip inception. Here, through direct measurements on various contacts involving elastomers or human fingertips, we show that the real contact area also decreases under shear, with reductions as large as 30%, starting well before macroscopic sliding. All data are captured by a single reduction law enabling excellent predictions of the static friction force. In elastomers, the area-reduction rate of individual contacts obeys a scaling law valid from micrometer-sized junctions in rough contacts to millimeter-sized smooth sphere/plane contacts. For the class of soft materials used here, our results should motivate first-order improvements of current contact mechanics models and prompt reinterpretation of the rate-and-state parameters.

area of real contact | rough contact | elastomer | static friction | rate-and-state friction

Rough solids in dry contact touch only at their highest asperities, so that real contact consists of a population of individual microjunctions (Fig. 1*B*), with a total area A^R. A^R is usually much smaller than the apparent contact area, A^A, that one would expect for smooth surfaces. Since the seminal work of Bowden and Tabor (1), it is recognized that the frictional properties of such multicontact interfaces are actually controlled by A^R rather than by A^A. In particular, direct measurements of A^R on transparent interfaces have been developed (2, 3) and repeatedly found proportional to the friction force, both for multicontacts (4–10) and for single contacts between smooth bodies (1, 11, 12), with the proportionality constant being the contact's frictional shear strength, σ. A^R is a dynamic quantity with three major causes for variations.

First, A^R is roughly proportional to the normal load applied to multicontacts (5, 6, 10). This result, which provides an explanation for Amontons–Coulomb's law of friction (friction forces are proportional to the normal force), has been reproduced by many models of weakly adhesive rough contacts under purely normal load (1, 4, 13–16). In the case of independent elastic microjunctions, although each of them grows nonlinearly with normal load, proportionality arises statistically due to randomness in the surface asperities' heights (13). Second, in static conditions, A^R slowly increases, typically logarithmically, with the time spent in contact (5, 17). This phenomenon, so-called geometric aging (18), is interpreted as plastic (5, 19, 20) or viscoelastic (21) creep at the microjunctions, depending on the materials in contact, and is different from contact strengthening with time at constant contact area (18, 22), so-called structural aging. Third, at the onset of sliding of the interface, the population of already aged microjunctions gradually slips and is replaced by new, smaller microjunctions. Slip inception is thus accompanied by a drop of A^R (5, 17), by up to a few tens of percent. This effect is often considered to be the origin of the difference between the peak (static) and steady sliding (kinematic) friction forces (18).

Accounting for these three dependencies together has been a major success in the science of friction because it provides a consistent picture of the physical mechanisms underlying the ubiquitous state-and-rate friction law (5, 18, 20–31), which is obeyed by multicontacts in a variety of materials, from polymer glasses to rocks, through rubber and paper. However, a series of experimental observations reported here and there in the literature over recent decades suggest that the picture may not be fully comprehensive yet. These observations, made on smooth contacts, have repeatedly indicated that the area of apparent contact, A^A, depends on the value of the tangential load, Q, applied to the interface. For instance, smooth metallic sphere/plane contacts typically grow as Q increases (1, 2), due to plastic deformations in the vicinity of the contact (1, 32). Conversely, A^A decreases when smooth elastomer-based sphere/plane contacts as well as fingertip contacts are increasingly sheared (9, 33–38), presumably due to viscoelastic and/or adhesion effects (33, 36, 38–40). It is therefore tempting to hypothesize that not only smooth but also rough interfaces have a dependence of their contact area on the tangential load, Q. Such a dependence would directly affect the resistance to sliding of a rough contact, the way we use current contact and friction models to predict the static friction force, and the physical meaning of the parameters of the rate-and-state friction law. To test this hypothesis, we carried out experiments to monitor, in multicontacts involving elastomers or human fingertips, the evolution of A^R when Q is increased from 0 to macroscopic sliding.

Significance

We investigate the origin of static friction, the threshold force at which a frictional interface starts to slide. For rough contacts involving rubber or human skin, we show that the real contact area, to which static friction is proportional, significantly decreases under increasing shear, well before the onset of sliding. For those soft materials, our results will impact how we use and interpret current contact mechanics and friction models.

Author contributions: J.S. designed research; R.S., G.P., C.D., I.E.B.A., S.A.A., and M.G. performed research; R.S., G.P., and J.S. analyzed data; and J.S. wrote the paper.

The authors declare no conflict of interest.

This article is a PNAS Direct Submission.

[1]To whom correspondence should be addressed. Email: julien.scheibert@ec-lyon.fr.

This article contains supporting information online at www.pnas.org/lookup/suppl/doi:10.1073/pnas.1706434115/-/DCSupplemental.

APPLIED PHYSICAL SCIENCES

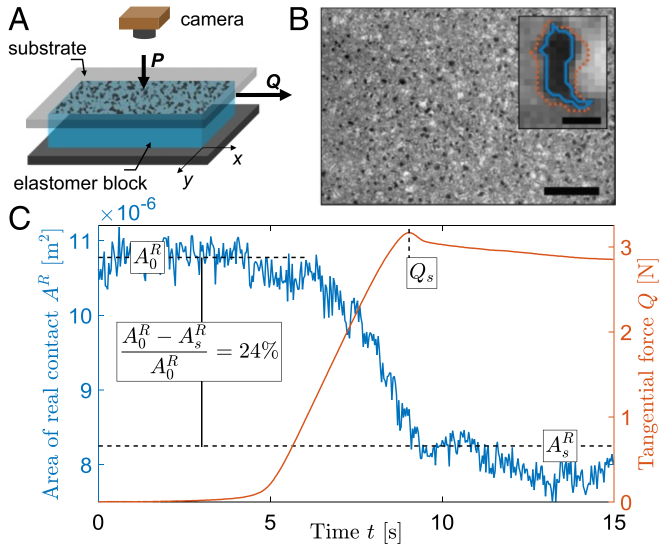

Fig. 1. Monitoring the area of real contact of elastomeric multicontact interfaces. (*A*) Sketch of the experiment. (*B*) Typical image of a PDMS/cross-linked PDMS multicontact. $A^R/A^A \simeq 2.05\%$. $R_q = 20$ µm. $P = 2.08$ N. (Scale bar: 1.87 mm.) (*B*, *Inset*) Zoom-in on a microjunction. Red (resp. blue): contour for $Q = 0$ (resp. under shear, at the onset of sliding). (Scale bar: 100 µm.) (*C*) Typical concurrent evolution of the area of real contact (blue) and the tangential force (red), of the multicontact interface shown in *B*, as a function of time (1 point of 10 shown). A_0^R (A_s^R): initial area (at static friction). Q_s: static friction force. $P = 2.08$ N. $V = 0.1$ mm/s.

Principle of the Experiments

Fig. 1*A* shows a sketch of the experimental setup configured for elastomeric contacts, similar to that used in ref. 41 (*Materials and Methods*). A slider made of a flat, smooth bare glass plate is placed in frictional contact onto a rough elastomer block [cross-linked polydimethylsiloxane (PDMS) rms roughness R_q) adhering to the table. The slider is driven horizontally, through a steel wire attached in the plane of the contact interface [to avoid torque buildup (42)], by a motorized linear stage moving along x at constant velocity V ranging from 0.05 mm$\cdot$s^{-1} to 1 mm$\cdot$s^{-1}. The normal load, P, is applied using dead weights in the range 0–7 N and the tangential force, Q, is monitored as the slider is driven toward macroscopic sliding. Noninvasive, in situ contact imaging is done in a light-reflected geometry by illuminating the interface from the top with a diffuse white light. Good contrast between real contact and out-of-contact regions is obtained due to heterogeneous reflection properties of the contact interface (Fig. S1): Real contact regions appear dark because light is transmitted through the transparent elastomer and absorbed by a black layer below the elastomer block; out of contact regions appear brighter because light is partly reflected by the glass/air dioptre and partly back scattered by the micrometer rough air/PDMS dioptre. Images of the interface are recorded with a CCD camera in synchronization with the tangential force. The images are efficiently binarized using automatic thresholding (*Materials and Methods*) to identify each microjunction (blue contour in Fig. 1*B*, *Inset*). The type of substrate (bare glass) is varied (*Materials and Methods*) by coating the slider's glass surface either with grafted PDMS chains or with a layer of cross-linked PDMS. We always start tangential loading 30 s after the contact has first been formed. Because the rate of geometrical aging becomes, in less than 10 s, negligible compared with the shear-induced variations of A^R described in the next section, it will have a negligible role in those variations. Also, the constant waiting time will ensure that structural aging, if active, will always affect the value of the static friction force in the same way and thus will not be responsible for its variations.

The Area of Real Contact Decreases Under Shear

Analysis of multicontact interfaces sheared toward macroscopic sliding revealed the typical behavior shown in Fig. 1*C*. The area of real contact, A^R, i.e., the sum of all individual areas of microjunctions, is found to decrease, by up to 30%, under increasing tangential force, Q. The reduction begins as soon as Q starts increasing and continues until the macroscopic sliding regime is reached, in which A^R remains roughly constant around its minimum. Similar observations were made irrespective of the interface type, roughness, normal load, and driving velocity. Note that no abrupt drop of the area of real contact is associated with the onset of sliding, when Q reaches Q_s.

Inspection of individual asperities (Fig. 1*B*, *Inset*) reveals that, under shear, most of them undergo a reduction of their area of real contact, showing that the macroscopic effect actually originates at the microjunction level. Note that since the glass surface is smooth, microjunctions formed under pure normal load remain in contact during shear.

Plotting A^R as a function of Q for different normal loads P applied to a multicontact (Fig. 2*A*) is an interesting way of identifying the law of area reduction. For all normal loads and all interface types, the decrease of A^R is found to be well fitted by an empirical quadratic law of the form

$$A^R(Q) = A_0^R - \alpha_R Q^2, \qquad \textbf{[1]}$$

with $A_0^R = A^R(Q = 0)$ the fitted initial area of real contact. A_0^R increases linearly with P (Fig. S2), which is classical for rough contacts. All dependences of the area reduction rate on system parameters are lumped into the fitting parameter α_R.

Onset of Sliding

The reduction in area of real contact stops soon after the tangential force has reached its maximum, the static friction force Q_s, which classically marks the onset of macroscopic sliding of the interface. The corresponding value of A^R is denoted A_s^R. Data corresponding to the macroscopic sliding regime cluster around a value of Q slightly smaller than Q_s. Interestingly, all points marking the onset of sliding in the $A^R(Q)$ plot in Fig. 2*A* align well on a straight line going through the origin. This shows that, for our multicontacts,

$$Q_s = \sigma A_s^R, \qquad \textbf{[2]}$$

with σ being the static contact's shear strength, which characterizes the frictional interaction between the two materials in contact (see *Materials and Methods* for values of σ for all interface types).

Introducing Eq. **2** in Eq. **1** leads to an expression of the relative area decrease along a given experiment: $(A_0^R - A_s^R)/A_s^R = \alpha_R \sigma^2 A_s^R$. This expression shows not only that the total area decrease is controlled by α_R, but also that the shear strength σ has a leading effect on it: The smaller σ is, the smaller the total area drop. This explains why, for PDMS/grafted PDMS interfaces which have the smallest σ (*Materials and Methods*), the area reduction remains small, making it difficult to evaluate α_R accurately.

Value of the Static Friction Force

Fig. 2*A* shows that the static friction force Q_s of our multicontacts is selected from the intersection of two behavior laws. First, Q_s obeys the threshold law given in Eq. **2**. Second, Q_s is related to the area of real contact through the reduction law $A_s^R = A_0^R - \alpha_R Q_s^2$. Solving for Q_s in this system of two equations yields

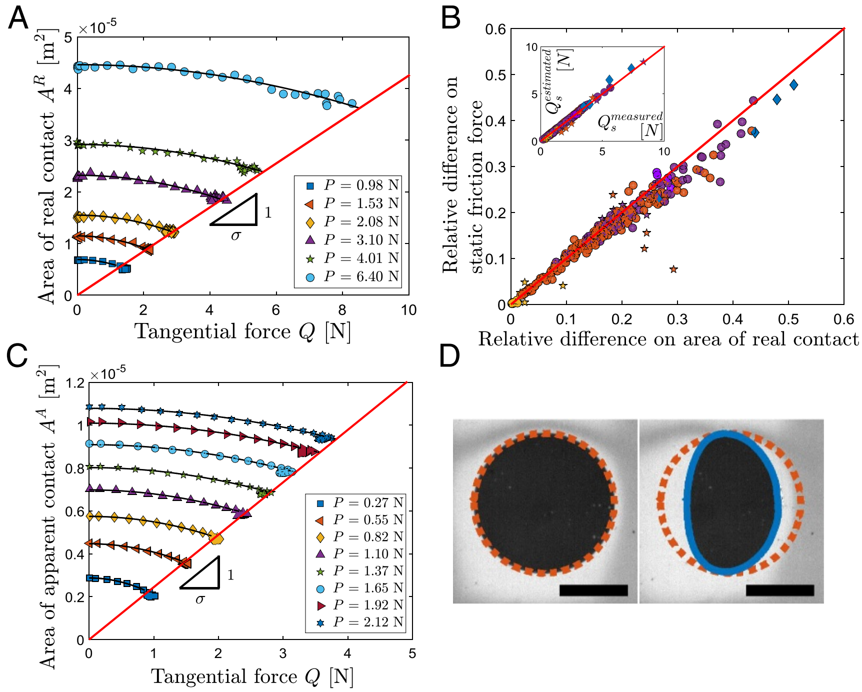

Fig. 2. Area reduction and static friction. (*A*) A^R vs. Q, for a PDMS/glass multicontact submitted to various normal loads P (1 point of 130 shown). $R_q = 26$ µm. $V = 0.1$ mm/s. Solid curves: quadratic fits of the form of Eq. **1**. Solid straight line: linear fit through data points corresponding to the onset of macroscopic sliding. See *Materials and Methods* for the value of σ. (*B*, *Inset*) Static friction force estimated using Eq. **3**, $Q_s^{estimated}$, vs. its measured value, $Q_s^{measured}$, for all experiments, including different velocities. (*B*, main plot) $(\sigma A_0^R - Q_s^{estimated})/\sigma A_0^R$, as a function of $(A_0^R - A_s^R)/A_0^R$. In both plots, the solid straight line has slope 1 and goes through the origin. Purple, PDMS/glass interfaces; yellow, PDMS/grafted PDMS; orange, PDMS/cross-linked PDMS; stars, multicontacts; circles, smooth sphere/plane contacts; blue diamonds, fingertip/glass contacts. $V = 0.1$ mm/s except light purple circles ($V =$ 0.05 mm/s, 0.1 mm/s, 0.5 mm/s, 1 mm/s for PDMS/glass at $P = 1.1$ N). (*C*) A^A vs. Q, for a smooth PDMS/glass sphere/plane contact, presented as in *A*. One point of 70 is shown. $R = 9.42$ mm. $V = 0.1$ mm/s. See *Materials and Methods* for the value of σ. (*D*) Images of the sphere/plane contact in *C* for $P = 0.55$ N. (*D*, *Left*) $Q = 0$. (*D*, *Right*) $Q = Q_s$. (Scale bars: 1 mm.)

$$Q_s = \frac{1}{2\alpha_R \sigma}\left(\sqrt{1 + 4\sigma^2 \alpha_R A_0^R} - 1\right). \qquad [3]$$

Fig. 2*B*, *Inset* represents, for all experiments (various types of interfaces, normal loads, velocities, roughness), the value of Q_s estimated by Eq. **3** as a function of its measured value. All points align on the equality line, showing good accuracy and robustness of our estimate. How much is Eq. **3** improving the estimate of Q_s with respect to the uninformed estimate, σA_0^R, made when one ignores the dependence of A^R with Q? To answer this, we plot in Fig. 2*B* (main plot) the relative difference between the two estimates as a function of the corresponding relative difference between A_s^R and A_0^R. Both differences are found roughly equal, showing that the observed area reductions, up to 30%, can lead to 30% overestimations (resp. underestimations) of Q_s (resp. σ) when the only available information about A^R is its initial value A_0^R.

This is practically important because most available models for the area of real contact in randomly rough contacts predict only A_0^R, as they consider interfaces under purely normal load (e.g., refs. 4, 13–16). A first-order improvement of these models would be to include the effect of incipient tangential loading and associated area reduction. They could then provide better estimates of the adhesive, purely interfacial, contribution to static friction quantified by σ. The viscoelastic, bulk contribution to friction would also be better estimated because the models would account for the reduced size of the microjunctions in the loading direction, which controls the excitation frequencies of the viscoelastic bodies.

A Common Behavior Across Scales

Now that our working hypothesis (in elastomers, the area of rough contacts, like that of smooth contacts, decreases with increasing shear) has been validated, we go farther and compare the reduction laws of A^R and A^A. To do this, we carried out additional experiments to measure A^A on smooth contacts between PDMS spheres of millimetric radius of curvature (*Materials and Methods*) and the same substrates previously used for rough contacts. Under increasing shear, those contacts start circular and progressively become ellipse-like, as classically found (33–36) (Fig. 2*D*). As far as the contact area is concerned, for all interface types, sphere/plane contacts behave exactly as multicontacts (compare Fig. 2*C* and 2*A*). In particular, the area reduction law is also captured by a quadratic form $A^A(Q) = A_0^A - \alpha_A Q^2$, identical to Eq. **1**, with α_A the reduction rate associated with the apparent area of individual contacts, as opposed to α_R related to the real area of multicontacts. The evolution of A_0^A with P is captured by the Johnson–Kendall–Roberts (JKR) model for adhesive sphere/plane contacts (43) (Fig. S3). The threshold law is again $Q_s = \sigma A_s^A$. The ingredients behind Eq. **3** being the same as for multicontacts, the estimate of Q_s for sphere/plane contacts is just as good (circles in Fig. 2*B*).

Such sphere/plane contacts are often considered good proxies for individual microjunctions in rough contacts. One advantage is that the tangential load can be measured directly for sphere/plane contacts, whereas it is inaccessible for an individual microjunction. This allows us to show, in Fig. 3 (circles), that for PDMS/glass sphere/plane contacts, α_A decreases with A_0^A as a power law with an exponent close to $-3/2$. We find it true for monocontacts of all types (Fig. S4).

To compare this behavior with that of individual microjunctions, we track, along each experiment, the area evolution of the individual microjunctions. Assuming they also obey a quadratic reduction law like Eq. **1**, their individual α_{Ai} are estimated as (*Materials and Methods*) $\alpha_{Ai} = (A_{0i}^A - A_{si}^A)/(\sigma^2 {A_{si}^A}^2)$, with σ the shear strength of the macroscopic contact. The α_{Ai} are plotted as a function of A_{0i}^A in Fig. 3 (squares). Strikingly, the dependence of α_A on the initial area, A_0^A, appears identical (power law of exponent around $-3/2$) within experimental accuracy for microjunctions and sphere/plane contacts, over four orders of magnitude of A_0^A. We find it true for interfaces of all types (Fig. S4).

Behavior of Fingertip Contacts

To illustrate the generality of our results, analogous experiments were carried out on biological contacts between human fingertips and bare glass (Fig. 4 and *Materials and Methods*). Real contact occurs only along the protruding fingerprint ridges (Fig. 4*C*) (37, 38, 44, 45). The evolution of the area of real contact is shown in

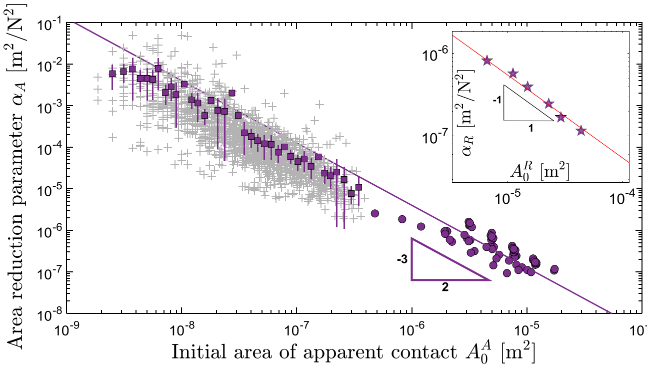

Fig. 3. Area reduction across scales: α_A vs. A_0^A (PDMS/glass interface). Circles: sphere/plane contacts for all R. V = 0.1 mm/s. $+$: raw data for microjunctions within multicontacts (R_q = 26 μm). Squares: average of the positive raw data divided into 40 classes. Bars show SD within each class. Line: guide for eyes with slope $-3/2$. *Inset*: α_R vs. A_0^R for the same multicontacts. *Inset* line: guide for eyes with slope -1.

Fig. 4*A* as a function of the tangential force applied, Q. Interestingly, A^R evolves under shear in a way very similar to that of elastomeric contacts (compare Fig. 4*A* with Fig. 2 *A* and *C*). First, we find that a quadratic reduction law like Eq. **1** captures reasonably the data (although a linear fit would also be acceptable). Second, we find a linear threshold law like Eq. **2**. As a consequence, Eq. **3** successfully predicts the value of the static friction force of fingertip contacts (blue diamonds in Fig. 2*B*).

As illustrated in Fig. 4*B*, we found that fingertip contacts under shear combine features of both sphere/plane contacts and planar multicontacts. As previously shown in the literature (37, 38), like sphere/plane contacts, their area of apparent contact (contours in Fig. 4*C*) decreases, by typically 40%. What we show here is that, simultaneously, the individual area of each microjunction also decreases, by about 10%. Both effects combine to give a reduction of about 45% of the area of real contact (45% $\simeq$ 40% + 10% of the remaining 60%).

Discussion

We now discuss the possible physical origins of the reduction in area of real contact and the quantities controlling the value of the reduction parameter α_R. As mentioned in the Introduction, reduction of the area of apparent contact A^A under shear has already been observed on smooth sphere/plane elastomeric contacts (33, 35, 36). Because we showed that A^A and A^R actually follow analogous reduction behaviors (Fig. 2 *A* and *C*), they may very well result from similar phenomena but at different scales. Two approaches have been proposed in the literature to interpret the observations on A^A.

The first approach focuses on the role of viscoelasticity, relating area reduction to the increase of elastic modulus of a viscoelastic body on which a rigid rough body is steadily sliding. This approach has been used both for smooth spherical (40, 46) and rough planar (14, 47) frictionless indentors and predicts a sliding-velocity–dependent amplitude of the area reduction. Note that in our experiments, α_A has a measurable, but weak velocity dependence. Loading-induced stiffening was also invoked to explain the apparent contact reduction in fingertip contacts (38). However, although in apparent agreement with our observations, the abovementioned viscoelastic models cannot explain them. The reason is that, in our experiments, the geometry is opposite: The rigid body is smooth and flat. Thus, in a steady sliding regime, the viscoelastic body (sphere or rough plane) experiences a deformation which is constant in time and thus is not affected by viscosity. In those conditions, the viscoelastic models would predict a recovery of the contact area to the value it had before shearing, i.e., under purely normal load. This is in striking contrast to our sphere/plane experiments, in which both the area and the shape of the steady sliding apparent contact remain significantly modified with respect to the initial situation (Fig. 2*D*). Additional experiments, in which shear loading is interrupted before the onset of sliding, show that, contrary to what viscoelastic models would have predicted, the area does not come back to its initial value. Those qualitative discrepancies suggest that viscoelasticity is not responsible for our observations.

The second approach focuses on the role of adhesion and describes the motion of the contour of sphere/plane contacts as a crack propagating under mixed-mode loading (opening plus shear). Unfortunately, all existing theoretical models (33, 36, 39) treat the case of axisymmetric shrinking of the contact area, an assumption which is strongly violated in our experiments (Fig. 2*D*). We believe that those models can anyway help us identify the mechanisms involved in the shear-induced area reduction. The two most recent models (36, 39) consider that the area reduction results from a combination of peeling at the contact's periphery (points in contact are lifted up from the glass) and microslipping in an annular peripheral region of the contact. To assess whether those mechanisms are involved in our experiments, we gently scratched an elastomer sphere to introduce small defects within the contact image that could be tracked during shearing experiments. Those experiments showed that for sphere/plane contacts, the area reduction is indeed related to both predicted contributions: (*i*) peeling at the trailing edge of the contact, partially compensated by the opposite behavior at the leading edge, collectively responsible for typically half of the total reduction, and (*ii*) compression of the contact in the loading direction due to heterogeneous slip, responsible for the other half of the reduction.

Given the good qualitative agreement of the adhesion-based models with our experiments, it is worth looking more quantitatively into their behavior. We carried out a numerical analysis of the model of ref. 36 and found that the beginning of the predicted area reduction is well fitted by a quadratic decay with the tangential load, in agreement with our observations. Independent variations of all model parameters allowed us to extract the scaling

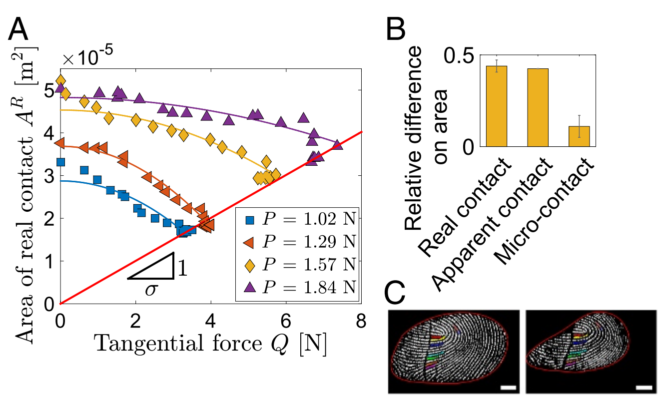

Fig. 4. Area reduction in human fingertip contacts. (*A*) A^R vs. Q, for various normal loads P (1 point of 190 shown). V = 0.1 mm/s. Curves: quadratic fits of the form of Eq. **1**. Line: linear fit through the data corresponding to the onset of macroscopic sliding, passing through origin. See *Materials and Methods* for the value of σ. (*B*) Relative area difference between initial and final contact. *B*, left: area of real contact, A^R (error bar: segmentation threshold modified by $\pm$3 gray levels). *B*, center: area of apparent contact, A^A (error bar: same as *B*, left). *B*, right: individual area of 10 selected microjunctions (colored in *C*) that remain in contact all along the experiment (error bar: $\pm$ SD). (*C*) Binarized image of a typical contact (P = 1.57 N). Red line: contour of the apparent area of contact. (Scale bar: 3 mm.) *C*, *Left*: Q = 0. *C*, *Right*: steady sliding.

relationship $\alpha_A \sim \frac{R^{0.18}}{E^{0.65} w_0^{0.47} P^{0.86}}$, with R the sphere's radius, E its Young's modulus, and w_0 the interface's work of adhesion. Interestingly, the exponent of the P dependence is close to -1. Considering that, for elastic sphere/plane contacts, P scales as $\left(A_0^A\right)^{3/2}$, this exponent is in good agreement with the exponent $-3/2$ found for individual contacts in Fig. 3. Although R was changed threefold and w_0 twofold, those ranges are not sufficiently large to test the corresponding scalings. The quite large negative exponent associated with E suggests that α_A becomes smaller when the contacting bodies are stiffer. This could explain why the reduction of the area of apparent contact under shear has mainly been reported for soft materials, like rubber or human skin, but not for instance for polymethylmethacrylate or glass (5, 17). It also suggests that in stiff plastic materials like metals, the area reduction is likely much smaller than the concurrent plasticity-induced growth of the area, explaining why only the latter has been reported. Although the model of ref. 36 appears scaling-wise consistent with our results on smooth spherical contacts, there is currently no available adhesion-based model for area reduction in rough contacts to compare with our data.

Irrespective of the precise mechanisms involved in area reduction, the phenomenon has important fundamental implications. First, we observed that (*i*) the reduction of area of real contact in rough contacts is the macroscale consequence of the shrinking of the individual microjunctions (Fig. 1*B*, *Inset*) and (*ii*) the reduction parameter α_A of microjunctions obeys a well-defined scaling law of the form $\alpha_A = \beta\left(A_0^A\right)^{-\gamma}$. Those two observations suggest that macroscale reduction could be understood from that of the microjunctions, through a statistical average, along the lines of previous statistical friction models (13, 48). In *SI Notes*, *Mean-Field Model Relating α_A and α_R*, we indeed derive the expression of the macroscale reduction parameter, α_R, in terms of the parameters of the microscale scaling law, β and γ, in the simple case of a multicontact made of identical, independent microjunctions. The main outcome of this mean-field approach is that the scaling of α_R with the initial area A_0^R is different from that of α_A. Within the assumptions used, we find that $\alpha_R \sim \left(A_0^R\right)^{-1}$, independent of the microscopic exponent γ. As shown in Fig. 3, *Inset*, this scaling actually captures very well the observed dependence of α_R with A_0^R for our macroscopic, rough contacts. Thus, it is now possible, for elastomers, to incorporate the shear-induced variations of the area of real contact in multiscale friction models like refs. 48–54, through the microscopic law $\alpha_A = \beta\left(A_0^A\right)^{-\gamma}$.

In the Introduction, we also argued that the success of the rate-and-state friction (RSF) law was due to the fact that it incorporates the three main recognized dependencies of the area of real contact. To what extent is the fourth dependency identified here affecting the way we understand the RSF law? The Rice–Ruina formulation of the RSF law (18, 24–26) involves a parameter, B, which is also the prefactor of the logarithmic increase of the static friction coefficient with the time spent at rest by the interface. If one neglects structural aging, such an increase is caused by the growth, in the same proportion, of the area of real contact due to asperity creep at rest (geometrical aging). Our results indicate that, at least for elastomers and human skin, before the static friction threshold is reached, the already aged area will decrease as the shear loading is increased. Thus, the area relevant to the static friction coefficient will be smaller than that expected if geometric aging was the only mechanism involved. As a consequence, interpreting the parameter B as a quantifier of geometrical aging alone leads, for those soft materials, to a systematic underestimation of the rate of geometrical aging of an interface (shown in *SI Notes*, *Reinterpretation of the Parameter B in the RSF Law*). We suggest that B instead represents a combination of the classical geometrical aging and of the shear-induced area variations, an idea already proposed for rocks (28). Our results are thus expected to directly impact (for the class of soft materials studied here) or inspire the many scientific fields in which friction and RSF in particular are useful, including tribology, earthquake/landslide science, and robot/human haptics.

Materials and Methods

Mechanical Aspects. Driving of the slider is obtained using a motorized translation actuator (Newport LTA-HL). The tangential force Q is measured using a stiff piezoelectric sensor (Kistler 9217A) placed close to the motor. The Q signals are digitized and recorded at a sampling rate of 3 kHz (1 kHz for sphere/plane contacts and fingertip contacts). The normal and tangential forces, P and Q, are measured with 0.1 mN and 1 mN accuracies, respectively. For planar rough contacts, the slider is driven through a horizontal steel wire of stiffness 9,700 $\pm$ 200 N/m. For sphere/plane contacts and fingertips, the slider is driven rigidly through the length of a cantilever beam of bending stiffness 52 $\pm$ 1 N/m. The elastomer blocks (35 $\times$ 20 $\times$ 2 mm^3 in *x,y,z* for R_q = 26 μm, 21 $\times$ 19 $\times$ 2 mm^3 for R_q = 20 μm) are made of PDMS (Sylgard 184, mass ratio 10:1) degassed during 1 h and cross-linked at ambient temperature during about 150 h. Its Poisson ratio is ν = 0.5 (incompressible material). Its Young's modulus is measured to be E = 1.6 $\pm$ 0.1 MPa [value (error bar): mean (SD) over all experiments using different spheres on PDMS/glass interfaces]. The rough free surface of each elastomer block is obtained by molding the polymer against a roughened steel plate. The height distribution of the steel plate was characterized with a tactile profilometer (Surfascan Somicronic) and found to be Gaussian, with a rms roughness R_q of either 20 μm or 26 μm. The smooth spherical PDMS caps used for sphere/plane contacts were obtained by molding against optically smooth concave optical lenses of radius R = 7.06 mm, 9.42 mm, or 24.81 mm.

Substrate Preparation.

Bare glass plates. Bare glass plates are obtained from Mirit Glas. Before experiments, the surface is washed with soapy water, then with ethanol, and eventually with distilled water. This process is repeated three times.

Glass coated with grafted PDMS chains. Microscope glass slides are cleaned by immersion in piranha solution [70/30 (vol/vol) of concentrated H_2SO_4 and H_2O_2) for 30 min at 50 °C. The solution is decanted, and the slides are rinsed with deionized water. They are then dried under a stream of N_2 gas, exposed to UV/ozone (cleaning plasma) oxidization for 6 min immediately before the deposition of organosilicon, and finally rinsed with ultrapure water. The entire cleaning process provides activated microscope glass slides, with clean and oxidized surfaces containing mainly Si-OH groups. A 100-mg/mL PDMS solution (in HPLC toluene) is passed through a microfilter to remove impurities. A drop of this solution is deposited onto an activated glass slide, which it is then spin-coated at 2,000 rpm for 30 s. The film is cured at 130 °C for 4 h. The surface is then rinsed in toluene for 2 h and dried with N_2. The resulting surface is covered with PDMS chains grafted at one end on the glass, with grafting density low enough for the rest of the chain to adsorb on the surface.

Glass coated with cross-linked PDMS. A PDMS elastomer base/curing agent mixture (mass ratio 10:1) of Sylgard 184 is poured into a mold composed of two glass plates separated by a polytetrafluoroethylene spacer either 1 mm (sample in Fig. 1) or 150 μm (sample in Figs. S2 and S4) thick. After cross-linking at room temperature for 150 h, one glass plate is peeled away, leaving the other with a smooth elastic coating to be used for friction experiments.

Interfacial Properties. The work of adhesion of each interface type involving PDMS was obtained by fitting $A_0^A(P)$ for sphere/plane contacts, using the JKR model (43). The data were obtained on a dedicated apparatus. We found w_0(PDMS/glass) = 27 $\pm$ 1 mJ/m^2 (agrees with ref. 36), w_0(PDMS/grafted) = 30 $\pm$ 1 mJ/m^2 (smaller than in ref. 12), and w_0(PDMS/cross-linked) = 65 $\pm$ 3 mJ/m^2 (larger than in ref. 55). The shear strengths of the various interface types were obtained as in Fig. 2*A*. For multicontacts, σ(PDMS/glass) = 0.23 $\pm$ 0.02 MPa (agrees with ref. 7), σ(PDMS/grafted) = 0.14 $\pm$ 0.02 MPa, and σ(PDMS/cross-linked) = 0.34 $\pm$ 0.05 MPa (coating thickness 1 mm). For sphere/plane contacts, σ(PDMS/glass) = 0.36 $\pm$ 0.01 MPa (agrees with ref. 56), σ(PDMS/grafted) = 0.07 $\pm$ 0.01 MPa (agrees with ref. 12), and σ(PDMS/cross-linked) = 0.23 $\pm$ 0.01 MPa (larger than in ref. 9).

Image Analysis. Images are recorded using a CCD camera (Flare 2M360 MCL, 8 bits, 2,048 $\times$ 1,088 square pixels) at 300 frames per second (100 frames per second for sphere/plane and fingertip contacts). The pixel size in multicontact images was typically 25 μm. Possible implications of this finite pixel size on area measurements are discussed in *SI Notes*, *Possible Implications of the Finite Optical Resolution of the Images*. To select the threshold used to binarize images, we used a method fully justified in *SI Notes*, *Contact Area*

Measurement, and summarized here. We fitted the intensity histogram of each image by a sum of two subhistograms: (*i*) one for the class of out-of-contact pixels (large intensities), the shape of which (distorted Gaussian) was inspired by the histogram of images fully out of contact, and (*ii*) one for the class of in-contact pixels (Gaussian). The threshold was taken at the intersection between the two subhistograms, which minimizes the probability to select a wrong class during thresholding. Along one experiment, the calculated threshold remains stable within ± 2 gray levels. It is thus taken as constant for each experiment at its mean value. It is found to increase by about 10 gray levels as the normal load increases from 1 N to 6 N. Tracking was performed as in ref. 57. To estimate α_{Ai} of microjunctions (Fig. 3), individual values of A^A_{0i} and A^A_{si} are the (nonquantified) initial and final values of the sigmoid fitted onto $A^A_i(t)$.

Fingertip Experiments. They were done similarly to those in ref. 45. The protocols were approved by the Board of Directors of the Laboratoire de Tribologie et Dynamique des Systèmes. The subject (one of the authors) gave his informed consent. The right forefinger (male, 24 y old, right-handed Caucasian) is pointing upward and constrained in a fixed position at about 30° from the surface (bare glass). The glass is pressed under constant normal load, in the range 1–2 N, and moved at constant speed $V = 0.1$ mm/s in the distal direction. Before each experiment, the fingertip is cleaned with ethanol using a nonwoven paper to limit dust contamination. The glass is cleaned the same as for PDMS/glass experiments. Each experiment starts after a waiting time of 1 min (time necessary for the contact size to stabilize). The shear strength of our fingertip/glass interfaces was measured to be $\sigma = 0.20 \pm 0.01$ MPa.

ACKNOWLEDGMENTS. We thank D. Bonamy, R. W. Carpick, D. K. Dysthe, T. Hatano, A. Malthe-Sørenssen, J. Penot, C. Putignano, and X. Tan for discussions. This work was supported by LABEX MANUTECH-SISE (ANR-10-LABX-0075) of Université de Lyon, within the program Investissements d'Avenir (ANR-11-IDEX-0007) operated by the French National Research Agency (ANR). It received funding from the People Program (Marie Curie Actions) of the European Union's Seventh Framework Program (FP7/2007–2013) under Research Executive Agency Grant Agreement PCIG-GA-2011-303871. We are indebted to Institut Carnot Ingénierie@Lyon for support and funding. We acknowledge funding through Projet International de Coopération Scientifique Grant 7422.

1. Bowden FP, Tabor D (1964) *The Friction and Lubrication of Solids* (Oxford Univ Press, Oxford).
2. Ovcharenko A, Halperin G, Etsion I (2008) In situ and real-time optical investigation of junction growth in spherical elastic–plastic contact. *Wear* 264:1043–1050.
3. Krick BA, Vail JR, Persson BNJ, Sawyer WG (2012) Optical in situ micro tribometer for analysis of real contact area for contact mechanics, adhesion, and sliding experiments. *Tribol Lett* 45:185–194.
4. Archard JF (1957) Elastic deformation and the laws of friction. *Proc R Soc Lond A* 243:190–205.
5. Dieterich JH, Kilgore BD (1994) Direct observation of frictional contacts: New insights for state-dependent properties. *Pure Appl Geophys* 143:283–302.
6. Rubinstein SM, Cohen G, Fineberg J (2004) Detachment fronts and the onset of dynamic friction. *Nature* 430:1005–1009.
7. Okamoto Y, Nishio K, Sugiura J, Hirano M, Nitta T (2007) Friction of elastomer-on-glass system and direct observation of its frictional interface. *J Phys Conf Ser* 89:012011.
8. Wu-Bavouzet F, Cayer-Barrioz J, Le Bot A, Brochard-Wyart F, Buguin A (2010) Effect of surface pattern on the adhesive friction of elastomers. *Phys Rev E* 82:031806.
9. Degrandi-Contraires E, Poulard C, Restagno F, Léger L (2012) Sliding friction at soft micropatterned elastomer interfaces. *Faraday Discuss* 156:255–265.
10. Yashima S, et al. (2015) Normal contact and friction of rubber with model randomly rough surfaces. *Soft Matter* 11:871–881.
11. Carpick RW, Salmeron M (1997) Scratching the surface : Fundamental investigations of tribology with atomic force microscopy. *Chem Rev* 97:1163–1194.
12. Cohen C, Restagno F, Poulard C, Léger L (2011) Incidence of the molecular organization on friction at soft polymer interfaces. *Soft Matter* 7:8535–8541.
13. Greenwood JA, Williamson JBP (1966) Contact of nominally flat surfaces. *Proc R Soc Lond A Math Phys Sci* 295:300–319.
14. Persson BNJ, Albohr O, Tartaglino U, Volokitin AI, Tosatti E (2005) On the nature of surface roughness with application to contact mechanics, sealing, rubber friction and adhesion. *J Phys Condens Matter* 17:R1–R62.
15. Pastewka L, Robbins MO (2014) Contact between rough surfaces and a criterion for macroscopic adhesion. *Proc Natl Acad Sci USA* 111:3298–3303.
16. Yastrebov VA, Anciaux G, Molinari JF (2015) From infinitesimal to full contact between rough surfaces: Evolution of the contact area. *Int J Solids Struct* 52:83–102.
17. Ben-David O, Rubinstein SM, Fineberg J (2010) Slip-stick and the evolution of frictional strength. *Nature* 463:76–79.
18. Baumberger T, Caroli C (2006) Solid friction from stick–slip down to pinning and aging. *Adv Phys* 55:279–348.
19. Dieterich JH (1972) Time-dependent friction in rocks. *J Geophys Res* 77:3690–3697.
20. Berthoud P, Baumberger T, G'Sell C, Hiver JM (1999) Physical analysis of the state- and rate-dependent friction law: Static friction. *Phys Rev B* 59:14313–14327.
21. Ronsin O, Coeyrehourcq KL (2001) State, rate and temperature-dependent sliding friction of elastomers. *Proc R Soc Lond A* 457:1277–1294.
22. Li Q, Tullis TE, Goldsby D, Carpick RW (2011) Frictional ageing from interfacial bonding and the origins of rate and state friction. *Nature* 480:233–236.
23. Dieterich JH (1979) Modeling of rock friction 1. Experimental results and constitutive equations. *J Geophys Res* 84:2161–2168.
24. Rice JR, Ruina AL (1983) Stability of steady frictional slipping. *J Appl Mech* 50:343–349.
25. Marone C (1998) Laboratory-derived friction laws and their application to seismic faulting. *Annu Rev Earth Planet Sci* 26:643–696.
26. Scholz CH (2002) *The Mechanics of Earthquakes and Faulting* (Cambridge Univ Press, Cambridge, UK).
27. Kawamura H, Hatano T, Kato N, Biswas S, Chakrabarti BK (2012) Statistical physics of fracture, friction, and earthquakes. *Rev Mod Phys* 84:839–884.
28. Nagata K, Nakatani M, Yoshida S (2012) A revised rate- and state-dependent friction law obtained by constraining constitutive and evolution laws separately with laboratory data. *J Geophys Res* 117:B02314.
29. Bar-Sinai Y, Spatschek R, Brener EA, Bouchbinder E (2014) On the velocity-strengthening behavior of dry friction. *J Geophys Res Solid Earth* 119:1738–1748.
30. Landes FP, Rosso A, Jagla EA (2015) Frictional dynamics of viscoelastic solids driven on a rough surface. *Phys Rev E* 92:012407.
31. Putelat T, Dawes JH (2015) Steady and transient sliding under rate-and-state friction. *J Mech Phys Solids* 78:70–93.
32. Brizmer V, Kligerman Y, Etsion I (2007) A model for junction growth of a spherical contact under full stick condition. *J Tribology* 129:783–790.
33. Savkoor AR, Briggs GAD (1977) The effect of tangential force on the contact of elastic solids in adhesion. *Proc R Soc Lond A Math Phys Sci* 356:103–114.
34. Varenberg M, Gorb S (2007) Shearing of fibrillar adhesive microstructure: Friction and shear-related changes in pull-off force. *J R Soc Interface* 4:721–725.
35. Petitet G, Barquins M (2008) *Matériaux Caoutchouteux* (Presses Polytechniques et Universitaires Romandes, Lausanne, Switzerland).
36. Waters JF, Guduru PR (2009) Mode-mixity-dependent adhesive contact of a sphere on a plane surface. *Proc R Soc A* 466:1303–1325.
37. André T, Lévesque V, Hayward V, Lefèvre P, Thonnard JL (2011) Effect of skin hydration on the dynamics of fingertip gripping contact. *J R Soc Interface* 8:1575–1583.
38. Delhaye B, Lefèvre P, Thonnard JL (2014) Dynamics of fingertip contact during the onset of tangential slip. *J R Soc Interface* 11:20140698.
39. Johnson KL (1996) Continuum mechanics modeling of adhesion and friction. *Langmuir* 12:4510–4513.
40. Carbone G, Putignano C (2013) A novel methodology to predict sliding and rolling friction of viscoelastic materials: Theory and experiments. *J Mech Phys Solids* 61:1822–1834.
41. Prevost A, Scheibert J, Debrégeas G (2013) Probing the micromechanics of a multi-contact interface at the onset of frictional sliding. *Eur J Phys E* 36:17.
42. Scheibert J, Dysthe DK (2010) Role of friction-induced torque in stick-slip motion. *EPL* 92:54001.
43. Johnson KL, Kendall K, Roberts AD (1971) Surface energy and the contact of elastic solids. *Proc R Soc Lond A* 324:301–313.
44. Scheibert J, Leurent S, Prevost A, Debrégeas G (2009) The role of fingerprints in the coding of tactile information probed with a biomimetic sensor. *Science* 323:1503–1506.
45. Prevost A, Scheibert J, Debrégeas G (2009) Effect of fingerprints orientation on skin vibrations during tactile exploration of textured surfaces. *Commun Integr Biol* 2:422–424.
46. Koumi KE, Chaise T, Nelias D (2015) Rolling contact of a rigid sphere/sliding of a spherical indenter upon a viscoelastic half-space containing an ellipsoidal inhomogeneity. *J Mech Phys Solids* 80:1–25.
47. Carbone G, Putignano C (2014) Rough viscoelastic sliding contact: Theory and experiments. *Phys Rev E* 89:032408.
48. Thøgersen K, Trømborg JK, Scheibert J, Sveinsson HA, Malthe-Sørenssen A (2014) History-dependent friction and slow slip from time-dependent microscopic junction laws studied in a statistical framework. *Phys Rev E* 89:052401.
49. Braun OM, Peyrard M (2008) Modeling friction on a mesoscale: Master equation for the earthquakelike model. *Phys Rev Lett* 100:125501.
50. Braun OM, Barel I, Urbakh M (2009) Dynamics of transition from static to kinetic friction. *Phys Rev Lett* 103:194301.
51. Trømborg JK, et al. (2014) Slow slip and the transition from fast to slow fronts in the rupture of frictional interfaces. *Proc Natl Acad Sci USA* 111:8764–8769.
52. Hulikal S, Bhattacharya K, Lapusta N (2015) Collective behavior of viscoelastic asperities as a model for static and kinetic friction. *J Mech Phys Solids* 76:144–161.
53. Trømborg JK, Sveinsson HA, Thøgersen K, Scheibert J, Malthe-Sørenssen A (2015) Speed of fast and slow rupture fronts along frictional interfaces. *Phys Rev E* 92:012408.
54. Amundsen DS, et al. (2015) Steady-state propagation speed of rupture fronts along one-dimensional frictional interfaces. *Phys Rev E* 92:032406.
55. Degrandi-Contraires E, et al. (2013) Cassie-Wenzel–like transition in patterned soft elastomer adhesive contacts. *EPL* 101:14001.
56. Nguyen DT, et al. (2011) Surface pressure and shear stress fields within a frictional contact on rubber. *J Adhes* 87:235–250.
57. Kelley D, Ouellette N (2011) Using particle tracking to measure flow instabilities in an undergraduate laboratory experiment. *Am J Phys* 79:267–273.

Supporting Information

Sahli et al. 10.1073/pnas.1706434115

SI Notes

Contact Area Measurement. In digital images of multicontact interfaces (e.g., Fig. 1*B*), real contact regions appear with low gray levels whereas out-of-contact regions correspond to higher gray levels. We can thus classify the pixels using a threshold on their gray level. The threshold value is determined automatically as explained in the following.

Maximum a posteriori thresholding. The idea is to formulate the thresholding as a two-class classification problem. A given pixel can belong to class C_1 of contact pixels or to class C_2 of out-of-contact pixels and we want to assign it the best class based on its gray level z. If we can build a conditional probabilistic model giving the probability of having one class given the gray level, the classification problem can be solved using the maximum a posteriori (MAP) decision rule.

Formally, we denote $p(C_1|z)$ (respectively $p(C_2|z)$) the probability for a pixel to be in class C_1 (respectively C_2) given its gray level z. The best class assignation $\hat{k}$ is given by

$$\hat{k} = \arg\max_{k\in\{1,2\}} p(C_k|z), \quad \textbf{[S1]}$$

with arg max the operator returning the argument of a function at its maximum.

In practice the posteriors $p(C_k|z)$ are not always available and Bayes' theorem is used to decompose them as

$$p(C_k|z) = \frac{p(C_k)p(z|C_k)}{p(z)}, \quad k \in \{1,2\}.$$

The evidence term $p(z)$ being independent from the classes, Eq. **S1** can be written as

$$\hat{k} = \arg\max_{k\in\{1,2\}} p(C_k)p(z|C_k). \quad \textbf{[S2]}$$

If the two conditional densities $p(z|C_k)$ (likelihoods) are unimodal, there exists a unique threshold level $\hat{z}$ such that

$$\begin{cases} p(C_1)p(z|C_1) < p(C_2)p(z|C_2) & \text{if } z < \hat{z} \\ p(C_1)p(z|C_1) \geq p(C_2)p(z|C_2) & \text{if } z \geq \hat{z} \end{cases}.$$

This threshold $\hat{z}$ is a solution of the equation

$$p(C_1)p(z|C_1) = p(C_2)p(z|C_2). \quad \textbf{[S3]}$$

Probabilistic model. To find the optimal threshold, we need to model the two terms of Eq. **S3**. These terms can be estimated from the image histogram, assuming a parametric model of the two classes C_1 and C_2. Indeed, the normalized histogram $h(z)$ of gray levels of an image to be segmented is an estimation of the probability density function $p(z)$ of gray levels in this image. Given the two pixel classes, we have

$$h(z) = p(C_1)p(z|C_1) + p(C_2)p(z|C_2). \quad \textbf{[S4]}$$

In Fig. S5*C*, we note the two modes of the histogram corresponding to the two terms of Eq. **S4**.

Parametric model. We choose to model each of the two classes by a parametric model inspired by the shape of the corresponding histograms. For the contact class, a Gaussian distribution is assumed,

$$G_{\mu,\sigma}(z) = \frac{1}{\sigma\sqrt{2\pi}} \exp - \frac{(z-\mu)^2}{2\sigma^2}, \quad \textbf{[S5]}$$

with σ the SD of the Gaussian and μ its mean. Note that σ may include second-order nonlinear effects of light transmission through air where the two solids are separated by a gap smaller than the light's wavelength.

For the noncontact class, an empirical distribution (distorted Gaussian) was inspired by the histogram of the images completely out of contact (Fig. S5*D*). Its form is given in Eq. **S6**,

$$F_{b,c,d}(z) = a \exp\left(\frac{z-b}{c}\right)^2 \log(1 + \exp 0.1(z-d)), \quad \textbf{[S6]}$$

with a a normalization parameter, c a parameter related to the SD of the distribution, b a parameter related to its mean, and d an adjustable parameter.

The histogram can then be written as

$$h(z) = \Pi_1 G_{\mu,\sigma}(z) + \Pi_2 F_{b,c,d}(z), \quad \textbf{[S7]}$$

with $p(C_1) = \Pi_1$, $p(C_2) = \Pi_2$, $p(z|C_1) = G_{\mu,\sigma}(z)$, and $p(z|C_2) = F_{b,c,d}(z)$.

Parameter estimation. Knowing the histogram of an image to be segmented, we can determine priors Π_1 and Π_2 and the parameters of the distributions by a least-squares fitting from Eq. **S7**. Once the parameters have been identified, the segmentation can be defined from the threshold obtained at the intersection of the two functions representing each term of Eq. **S7**.

Threshold. The position of the intersection is given immediately as an output of the adjustment process, with an accuracy of ± 3 gray levels (green line in Fig. S5*C*). Along an experiment, i.e., considering all the images one by one, we found that the threshold calculated this way remains stable within ± 2 levels of gray. Given this stability, we have chosen to use a fixed threshold for all images of the same experiment. This threshold is obtained as an average over all individual thresholds along the experiment. It is found to increase by about 10 gray levels as the normal load increases from 1 N to 6 N.

Fig. S5 *E* and *F* shows the results of the segmentation of images in Fig. S5 *A* and *B*, respectively, using the above-described method. White spots correspond to microjunctions. The great resemblance between the black spots of the image in Fig. S5*A* and the white spots in Fig. S5*E*, together with the quasi-absence of white spots in Fig. S5*F*, validates the adopted segmentation method. More quantitatively, if the image in Fig. S5*A* is segmented using the extremal values of the likelihood interval of the threshold over time (typically $X \pm 3.5$ with X around 50), we find that the relative variation on the contact area is lower than 7.7% between min and max.

Mean-Field Model Relating α_A and α_R. Greenwood and Williamson's model (13) describes a rough surface as a collection of independent spherical asperities, all with the same radius of curvature R and with a random height distribution with SD s. In the case of an exponential distribution, Baumberger and Caroli (18) observed that the average area of a microjunction is $\overline{A_0^{A,m}} = \pi R s$, independent on the normal load. As a consequence, the number of microjunctions involved in the multicontact grows linearly with the total area of real contact.

Based on these observations, we consider a mean-field model in which multicontacts are made of N identical, independent microjunctions of individual initial area $\overline{A_0^{A,m}}$, such that the initial macroscopic area of real contact is $A_0^R = N\overline{A_0^{A,m}}$. Based on the results of Fig. 2*C*, we further assume that, when the interface is sheared with a tangential force Q, each microjunction obeys a quadratic area reduction law of the form

$\overline{A^{A,m}} = \overline{A_0^{A,m}} - \alpha_A q^2$, with $q = Q/N$ and α_A the tangential load applied on and the area reduction parameter of each individual microjunction, respectively. Finally, based on the scaling law in Fig. 3, we also assume that $\alpha_A = \beta \overline{A_0^{A,m}}^{\gamma}$.

The macroscopic area reduction law will then be obtained by rewriting the expression $A^R = N\overline{A^{A,m}}$,

$$A^R = N\left(\overline{A_0^{A,m}} - \beta\overline{A_0^{A,m}}^{\gamma} q^2\right) \quad \text{[S8]}$$

$$= N\overline{A_0^{A,m}} - N\beta\overline{A_0^{A,m}}^{\gamma}\frac{Q^2}{N^2} \quad \text{[S9]}$$

$$= A_0^R - \beta\frac{\overline{A_0^{A,m}}^{\gamma}}{N}Q^2 \quad \text{[S10]}$$

$$= A_0^R - \beta\frac{\overline{A_0^{A,m}}^{\gamma+1}}{A_0^R}Q^2, \quad \text{[S11]}$$

meaning that $\alpha_R = \beta_R\left(A_0^R\right)^{-1}$, with $\beta_R = \beta\overline{A_0^{A,m}}^{\gamma+1}$ being a constant independent of A_0^R (and of P). The obtained scaling ($\alpha_R \sim (A_0^R)^{-1}$) is in good agreement with the data shown in Fig. 3, *Inset*.

Reinterpretation of the Parameter *B* in the RSF Law. The Rice and Ruina formulation of the RSF law (23) is usually given as (18, 25, 26)

$$\mu(V,\theta) = \mu_0 + A ln\left(\frac{V}{V_0}\right) + B ln\left(\frac{V_0\theta}{D_c}\right), \quad \text{[S12]}$$

$$\dot{\theta} = 1 - \frac{V\theta}{D_c}, \quad \text{[S13]}$$

with V the sliding velocity, V_0 an arbitrary reference velocity, D_c a critical slip length, and θ a state variable.

In the static case ($V = 0$), $\theta = t$, so for long hold times we have

$$\frac{d\mu_s}{d(ln(t))} = B, \quad \text{[S14]}$$

with $\mu_s = \frac{Q_s}{P} = \frac{\sigma A_s^R}{P}$ the static friction coefficient.

If one assumes that geometrical aging is the only mechanism involved in the selection of the area of real contact, Eq. **S14** could be integrated as

$$A_{s,aging}^R(t) = A_0^R + \frac{PB_{aging}}{\sigma}ln\,(t). \quad \text{[S15]}$$

Let us instead assume that after aging until time t, shear loading starts to be applied. The area of real contact of the aged interface, given by Eq. **S15**, corresponds to the initial area for the shear-induced reduction phenomenon. Assuming that shear loading is so fast that the additional geometrical aging is negligible during the time interval required to shear the interface from rest to the onset of sliding, Eq. **3** can be rewritten as

$$Q_s = \frac{1}{2\alpha_R\sigma}\left[\sqrt{1 + 4\alpha_R\sigma^2\left(A_0^R + \frac{PB_{aging}}{\sigma}ln\,(t)\right)} - 1\right]. \quad \text{[S16]}$$

Using Eq. **S14**, the parameter B can now be evaluated from the derivative of Q_S with respect to $ln(t)$, which gives

$$B = \frac{1}{P}\frac{dQ_s}{d(ln(t))} = \frac{B_{aging}}{\sqrt{1 + 4\alpha_R\sigma^2\left(A_0^R + \frac{PB_{aging}}{\sigma}ln\,(t)\right)}}. \quad \text{[S17]}$$

Noting that $\sqrt{1 + 4\alpha_R\sigma^2\left(A_0^R + \frac{PB_{aging}}{\sigma}ln\,(t)\right)} = 1 + 2\alpha_R\sigma^2 A_s^R$ (replace Q_s with σA_s^R in Eq. **S16** and reorganize), we can rewrite Eq. **S17** as

$$B = \frac{B_{aging}}{1 + 2\alpha_R\sigma^2 A_s^R}. \quad \text{[S18]}$$

Eq. **S18** directly shows that, due to shear-induced area reduction, B is always smaller than the value that one would expect (B_{aging}) if geometrical aging was the only mechanism at play. In other words, interpreting B as a direct quantifier of geometrical aging alone amounts to underestimating the rate of aging at the interface. To get a better sense of how much the underestimation is, remember that $\alpha_R\sigma^2 A_s^R$ corresponds to the relative area reduction due to shear (*Onset of Sliding* in main text). We have observed relative area reductions up to about 30%, so that the denominator of Eq. **S18** can be up to about 1.6, meaning that the rate of aging may be underestimated by up to about 40%.

Possible Implications of the Finite Optical Resolution of the Images. The optical resolution of any digital image is limited to the pixel lateral size s, typically 25 μm in our multicontact images. As a consequence, any structure of the area of real contact with a length-scale smaller than s cannot be resolved. This limitation may affect our measurements of A^R in two ways.

First, patches of real contact may contain holes that are out of contact and smaller than s^2. This effect would lead to an overestimation of A^R. To assess whether this case is frequent, we considered typical microjunctions and imaged them with different zoom magnitudes (see Fig. S6 for a typical example). When reducing the pixel size by a factor of 3 (maximum zoom available with our optical device), i.e., by reducing the pixel area by about one order of magnitude, we uncovered very few holes, so that the area measurement of microjunctions was virtually unaffected by the change of resolution. The fact that only few holes can be observed is qualitatively consistent with the low Young's modulus of PDMS which, under the action of adhesive stress, will easily deform to conform to the rigid substrate.

The second effect is that microjunctions with an area smaller than $A_{pix} = s^2$ have a low probability to be detected, leading to an underestimation of A^R. To quantify the missing area due to this effect, we characterized the probability density function (pdf) of the areas of individual microjunctions in unsheared interfaces, A_{0i}^A. We found that, for all normal loads, those pdfs are reasonably fitted by power laws, i.e., with a form $p(A_{0i}^A) = K(A_{0i}^A)^{-n}$. Assuming that this form is valid at all scales between 0 and the maximum microjunction size, $A_{0i,max}^A$, we can assess what the fraction is of the area that is constituted by microjunctions smaller than A_{pix}. The total area is given by

$$A_0^R = \int_0^{A_{0i,max}^A} A_{0i}^A p(A_{0i}^A)\,dA_{0i}^A = K\frac{(A_{0i,max}^A)^{2-n}}{2-n}, \quad \text{[S19]}$$

while the area missed due to the finite size of the pixels is

$$A_{0,missed}^R = \int_0^{A_{pix}} A_{0i}^A p(A_{0i}^A)\,dA_{0i}^A = K\frac{(A_{pix})^{2-n}}{2-n}. \quad \text{[S20]}$$

Finally, the fraction of missed area is $\frac{A_{0,missed}^R}{A_0^R} = \frac{(A_{pix})^{2-n}}{(A_{0i,max}^A)^{2-n}}$. With n found close to 1.5 and $A_{0i,max}^A$ being larger than 100 A_{pix}, we estimate that $\frac{A_{0,missed}^R}{A_0^R} \simeq \sqrt{\frac{A_{pix}}{A_{0i,max}^A}} < \frac{1}{10}$. This means that, in our experiments, the fraction of the area constituted by microjunctions smaller than the pixel size is always smaller than 10%

and is usually smaller than 5%. This fraction is of the order of or smaller than that associated to the uncertainty on A^R due to the determination of the segmentation threshold. Note that such an error is an absolute error and can affect the measured value of σ, by the same fraction. In contrast, the evolution of the area under shear relative to the initial area is essentially unaffected by this absolute error and thus does not affect the main conclusions of the present study.

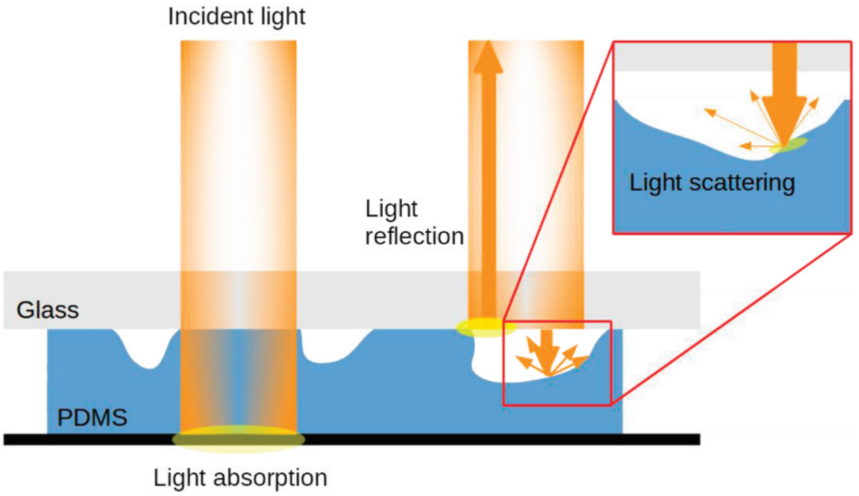

Fig. S1. Sketch of the light behavior at the interface. A rough PDMS sample (blue) in contact with a smooth glass plate (gray) is illuminated from the top by a diffuse white light. The light rays can be either transmitted through the real contact regions and absorbed by a black layer (bottom) or partly reflected by the glass/air dioptre and partly back scattered by the air/PDMS dioptre in out-of-contact regions.

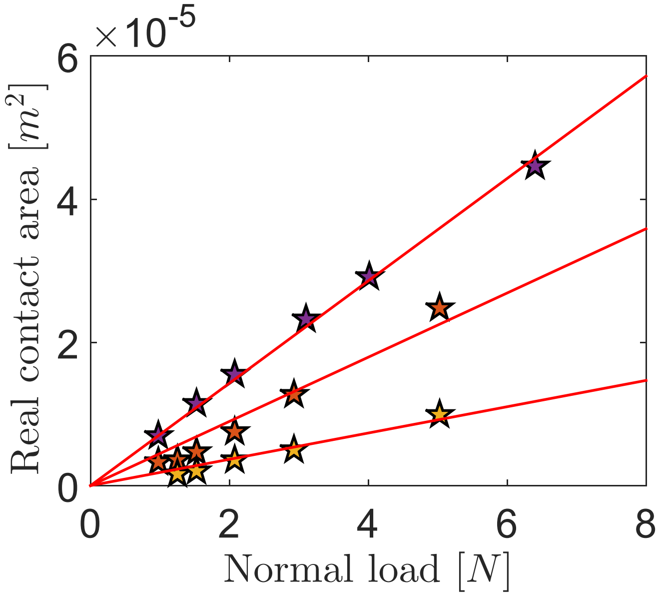

Fig. S2. Initial area of real contact is proportional to the normal load for multicontacts. Real contact area (for $Q = 0$) as a function of the normal load is shown. Purple: PDMS/glass multicontacts ($R_q = 26$ μm). Orange: PDMS/cross-linked PDMS multicontacts ($R_q = 20$ μm). Yellow: PDMS/grafted PDMS multicontacts ($R_q = 20$ μm). Red lines: linear fits passing through the origin.

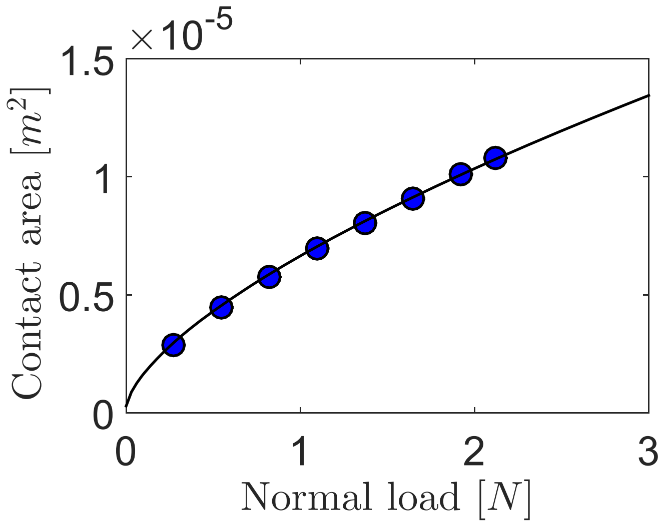

Fig. S3. Initial area of apparent contact is captured by the JKR model for sphere/plane contacts (43). Shown is apparent contact area (for $Q = 0$) as a function of the normal load, for the experiments shown in Fig. 2*C*. Solid line: prediction of the JKR model with $\nu = 0.5$, $w_0 = 27\ \mathrm{mJ/m^2}$, $R = 9.42$ mm, and $E = 1.9$ MPa. Note that, as mentioned in *Materials and Methods*, the value of w_0 was obtained separately using a dedicated apparatus.

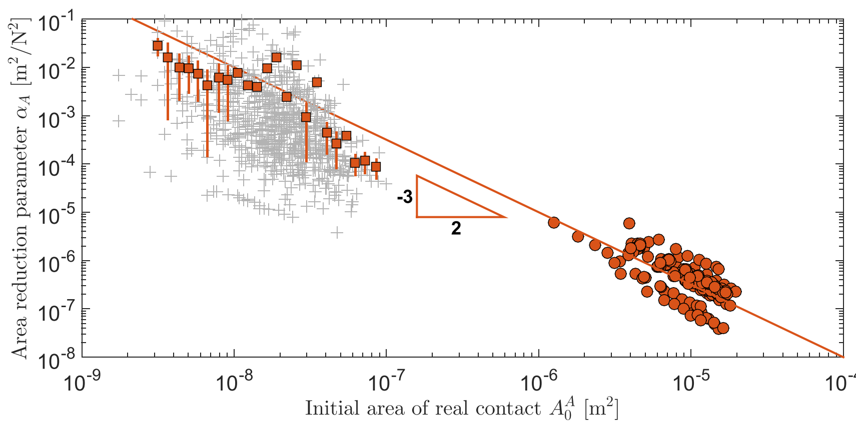

Fig. S4. Area reduction across the scales. Shown is α_A as a function of A_0^A (PDMS/cross-linked PDMS type of interface, coating thickness 150 μm, $\sigma = 0.30 \pm 0.01$ MPa). Circles: sphere/plane contacts. $R = 9.42$ mm. $V = 0.1$ mm/s. Gray crosses: raw data for microjunctions within multicontacts. Squares: average of the raw data divided into 23 classes. Error bars: SD within each class. Solid line: guide for eyes with slope $-3/2$.

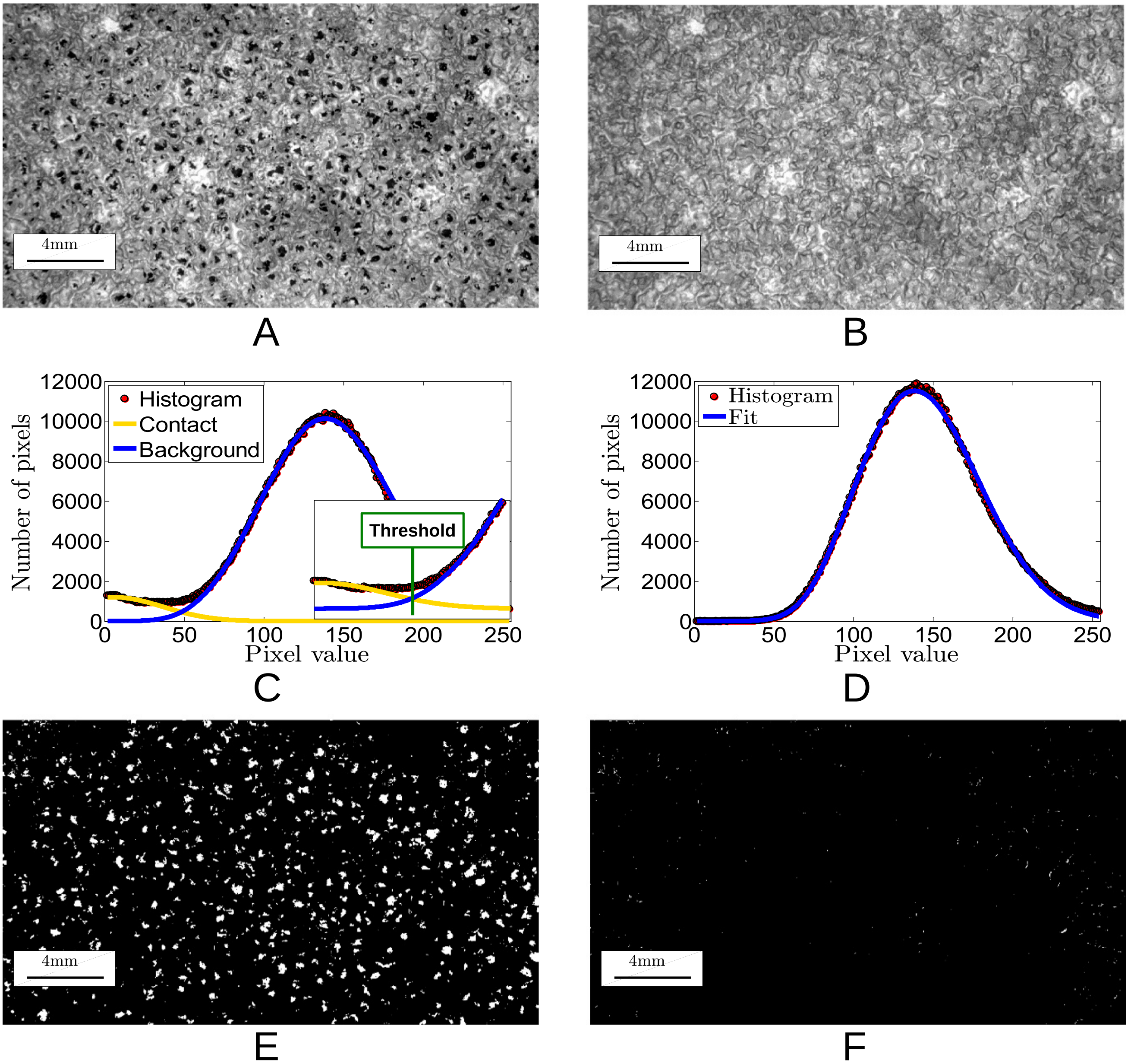

Fig. S5. Principle of the image segmentation. Shown is an example of a PDMS/glass multicontact, with $R_q = 26$ μm. (*A*) Raw contact image. (*B*) Raw non-contact image serving as a calibration for the shape of the out-of-contact histogram distribution. (*C*) Contact image histogram. (*D*) Out-of-contact image histogram. (*E*) Binarized contact image. (*F*) Binarized out-of-contact image.

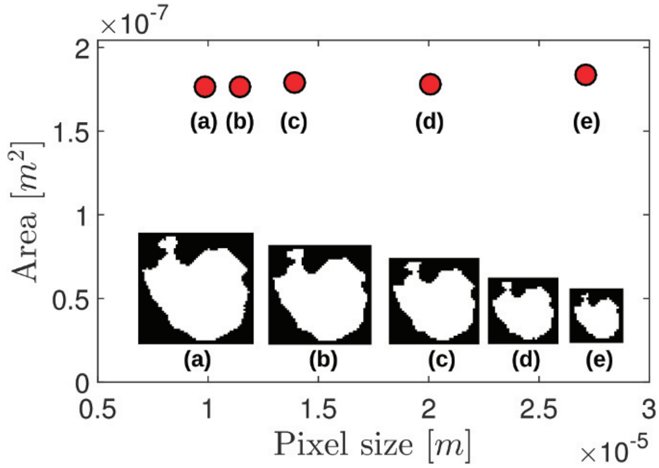

Fig. S6. Area measurements are essentially scale independent. Main plot (red circles) shows measured area of a microjunction as a function of the pixel size. *Insets a–e* show a segmented image of the same microjunction for various zoom-ins.